

## Chiral magnetism, lattice dynamics, and anomalous Hall conductivity in $V_3AuN$ antiferromagnetic antiperovskite

J. M. Duran-Pinilla 


*School of Physics, FICOMACO Research Group, Universidad Industrial de Santander,  
Carrera 27 Calle 09, 680002 Bucaramanga, Colombia*

Aldo H. Romero \*

*Department of Physics and Astronomy, West Virginia University, Morgantown, West Virginia 26506-6315, USA  
and Department of Physics and Materials Science, University of Luxembourg, 1511 Luxembourg, Luxembourg*

A. C. Garcia-Castro †

*School of Physics, CIMBIOS Research Group, Universidad Industrial de Santander,  
Carrera 27 Calle 09, 680002 Bucaramanga, Colombia*

 (Received 29 July 2022; revised 29 October 2022; accepted 2 December 2022; published 19 December 2022)

Antiferromagnetic antiperovskites, where magnetically active 3d metal cations are placed in the octahedral corners of a perovskite structure, are in the spotlight due to their intertwined magnetic structure and topological properties. Especially their anomalous Hall conductivity, which can be controlled by applied strain and/or electric field, makes them highly attractive in different electronic applications. Here, we present the study and theoretical understanding of an antiperovskite compound that can offer enormous opportunities in a broad set of applications. Using first-principles calculations, we investigated the structure, lattice dynamics, noncollinear magnetic ordering, and electronic behavior in the vanadium-based antiperovskite  $V_3AuN$ . We found an antiperovskite structure centered on N similar to the  $Mn_3AN$  family as the structural ground state. In such a phase, a  $Pm\bar{3}m$  ground state was found in contrast to the  $Cmcm$  post-antiperovskite layered structure, as in the  $V_3AN$ ,  $A = Ga, Ge, As, \text{ and } P$ . We studied the lattice dynamics and electronic properties, demonstrating its vibrational stability in the cubic structure and a chiral antiferromagnetic noncollinear ordering as a magnetic ground state. Finally, we found that the anomalous Hall conductivity, associated with the topological features induced by the magnetic symmetry, is  $\sigma_{xy} = -291 \text{ S cm}^{-1}$  ( $\sigma_{111} = -504 \text{ S cm}^{-1}$ ). The latter is the largest reported in the antiferromagnetic antiperovskite family of compounds.

DOI: [10.1103/PhysRevMaterials.6.125003](https://doi.org/10.1103/PhysRevMaterials.6.125003)

### I. INTRODUCTION

The antiperovskite structures exhibit a broad and diverse set of unconventional physical and chemical properties generated by the comprehensive structural features inherited from their counterpart perovskites [1–3]. Among them, the  $Mn_3AN$  family ( $A = Ni, Cu, Zn, Ga, Ge, Pd, In, Sn, Ir, \text{ and } Pt$ ) has shown remarkable properties that cover temperature-dependent magnetic and structural transitions [4], frustrated noncollinear ordering [5], large spin-phonon coupling [6], barocaloric response [7], strain tunability of the magnetic response [8], giant piezomagnetism and magnetostriction [8–11], and electrical control of their topological properties [12,13]. All the latter features are strongly intertwined with the magnetic structure and related symmetry operations. Regarding the magnetic response, most of the theoretical and experimentally focused efforts have been dedicated to the  $Mn_3AN$  family, leaving aside novel and unexplored materials

with possible enhanced properties but with different magnetic cations. Recently, some efforts have been dedicated to the  $Cr_3AN$  family, showing strong magnetostructural coupling, noncollinear magnetic ordering, and tangible topologically related properties [14]. Along these lines, the vanadium-based antiperovskite family,  $V_3AN$ , has also been studied and some examples reported ( $A = Ga, Ge, As, \text{ and } P$ ). In particular, the cases with  $A = P$  and  $As$  have been experimentally analyzed and superconducting behavior was observed [15]. Nevertheless, unlike in the  $Mn_3AN$  and  $Cr_3AN$  cases, the reported  $V_3AN$  materials belong to the layered orthorhombic anti-postperovskite structure  $Cmcm$  (SG 63) [16–19]. This anti-postperovskite is far from the cubic symmetry shown by its Mn-based counterparts, where the crystal symmetry and magnetic ordering couple to give rise to the topological properties. Therefore, to expand the candidates of cubic antiperovskites, where the formation of kagome lattices is crucial to the emergence of magnetic ordering and topological properties [12,20], more efforts and studies are needed to discover novel antiperovskite candidates among other families of compounds. For instance, it is expected that similar cubic antiperovskite compounds exist among this family, in which

\*aldo.romero@mail.wvu.edu

†acgarcia@uis.edu.co

topological properties associated with intertwined magnetic structure and their symmetry can be present. Moreover, the  $V_3AN$  family offers an additional advantage based on its large vanadium radius ( $r_V = 171$  pm [21]) at the octahedral corner site, compared to Mn ( $r_{Mn} = 161$  pm [21]), potentially allowing the incorporation of larger and heavier elements as cell corner sites and maintaining the noncollinear magnetic response. The latter is highly desirable considering that strong spin-orbit coupling is a key ingredient to enlarged topologically related properties, as in the case of the anomalous Hall conductivity [14]. Furthermore, to make this type of compound even more attractive, large topological properties and possible electrical tuning are expected for noncollinear spintronics applications [22,23]. As such, in this study, we theoretically propose, based on the perovskite structural criteria, a candidate among the antiperovskite  $V_3AN$  family. Herewith, we explain the atomic size relationship and tolerance conditions for an antiperovskite to hold the cubic  $Pm\bar{3}m$  (SG 221) symmetry. Furthermore, this structure can allocate a heavy metallic element as a cell corner site, providing a robust spin-orbit coupling to the kagome lattice and enhancing the electronic properties. Thus, we demonstrate and explain the ground state structure by showing the structural stability from the phonon spectra, considering the antiferromagnetic noncollinear ordering. Consequently, we explored its allowed noncollinear magnetic orderings that result in nonzero magnetic vector chirality and found that in terms of the magnetocrystalline anisotropy energy, the magnetic structure of the ground state symmetry shows a  $\Gamma_{4g}$  chiral magnetic ordering. The latter is allowed by symmetry, and the presence of tangible Berry curvature is also demonstrated in our work. Finally, such a magnetic noncollinear ordering coupled to a robust spin-orbit coupling provided by the Au sites, embedded into the kagome lattice, induces one of the most considerable anomalous Hall conductivities obtained in the antiperovskite family of materials.

## II. COMPUTATIONAL AND THEORETICAL DETAILS

We used density functional theory (DFT) [25,26] calculations to compute all properties reported here by using the VASP code (version 5.4.4) [27,28]. The projected-augmented wave approach, PAW [29], was used to represent the valence and core electrons. The electronic configurations considered in the pseudopotentials as valence electrons are V ( $3p^63d^44s^1$ , version 07Sep2000), Au ( $5d^{10}6s^1$ , version 04Oct2007), and N ( $2s^22p^3$ , version 08Apr2002). The exchange correlation was represented within the generalized gradient approximation (GGA-PBEsol) parametrization [30] and the V:3d electrons were corrected through the DFT +  $U$  approximation within the Liechtenstein formalism [31]. We used a Coulomb repulsion parameter  $U = 1.2$  eV that was optimized to reproduce the electronic structure, and the lattice parameter reported by Rieger *et al.* [32]. The observables to compare with were also obtained within the metaGGA exchange-correlation formalism [33] calculation in the SCAN representation [34]; see Fig. S1 in the Supplemental Material [35]. Moreover, the magnetic moment was also compared with that obtained by means of the HSE06 hybrid functional-based calculation [36]. It is worth mentioning

that the hybrid functional-based calculations, as well as the metaGGA results, show a rather large magnetic moment per V atom in the  $V_3AuN$  ( $m > 1.2 \mu_B \text{ atom}^{-1}$ ). Nonetheless, in the absence of the Coulomb  $U$  correction, the magnetic moment per V atom is in the range of weak magnetism ( $m = 0.024 \mu_B \text{ atom}^{-1}$ ). A tangible magnetic moment can be obtained in the PBEsol +  $U$  for  $U$  values above 0.4 eV; see Fig. S1 in Supplemental Material [35]. The periodic solution of the crystal was represented by using Bloch states with a Monkhorst-Pack [37]  $k$ -point mesh of  $13 \times 13 \times 13$  and 600 eV energy cutoff to give a force convergence of less than  $0.001 \text{ eV \AA}^{-1}$  and energy less than 0.1 meV. Spin-orbit coupling (SOC) was included to describe the noncollinear magnetic configurations correctly [38]. The thermal stability of the compound under different noncollinear magnetic orderings was tested by computing the phonon-dispersion curves, which were obtained using the finite-displacement approach [39,40]. Phonon dispersions were postprocessed with the PHONOPY code [41]. To obtain the anomalous Hall conductivity and Berry curvature, we used the Wannier function methodology for which the Wannierization was performed with the WANNIER90 code [42,43] and postprocessed with the WANNIERRI package [44]. Here,  $s$ ,  $p$ , and  $d$  orbitals were considered in the V and Au cases, while  $s$  and  $p$  were considered at the N site. Additionally, a 6.0 eV window was used around the Fermi level for the Wannierization. Finally, the atomic structure figures were elaborated with the VESTA code [45].

## III. RESULTS AND DISCUSSION

As a result of a structural search over novel antiperovskite compounds within the  $M_3AN$  family, we found as a potential candidate the  $V_3AuN$  compound [32,46]. This structural search was performed within the Materials Project database [47] and the ICSD database [48,49]. The performed constrain search imposed a fixed cubic  $Pm\bar{3}m$  symmetry and magnetically active  $3d$  metal cations in the octahedral  $M$  site added to nitrogen and  $4d/5d$  heavy metal cations expected to occupy the octahedral center and corner cell  $A$  sites. Figure 1(a) depicts the Au- and N-centered  $Pm\bar{3}m$   $V_3AuN$  antiperovskite structures where the octahedra are formed by the V atoms. Here, in the Au-centered case, reported in Ref. [46], the total energy for the spin-polarized FM ordering is  $E = -26.907 \text{ eV f.u.}^{-1}$  whereas, in the former N-centered antiperovskite, the total energy in the FM ordering is  $E = -40.917 \text{ eV f.u.}^{-1}$  representing a difference in energy of  $\Delta E = -14.010 \text{ eV f.u.}^{-1}$  in favor of the N-centered structure. This considerable difference in the total energy suggests the regular N-centered antiperovskite is potentially the ground state of this material, also observed in the  $Mn_3AN$  family [50,51]. Such a result is in apparent contradiction with the literature-reported structure [46], which claims a Au-centered type perovskite-like structure belonging to the  $Pm\bar{3}m$  structure. However, this N-centered structure agrees with Rieger *et al.* [32] who reported the existence of  $V_3AuN$  belonging to the cubic perovskite symmetry with lattice parameters of  $a = 3.962 \text{ \AA}$  within the  $Pm\bar{3}m$  space group [32]. For instance, the latter structure follows the same crystalline arrangement observed in antiperovskite-like materials such as  $Mn_3AN$ ,

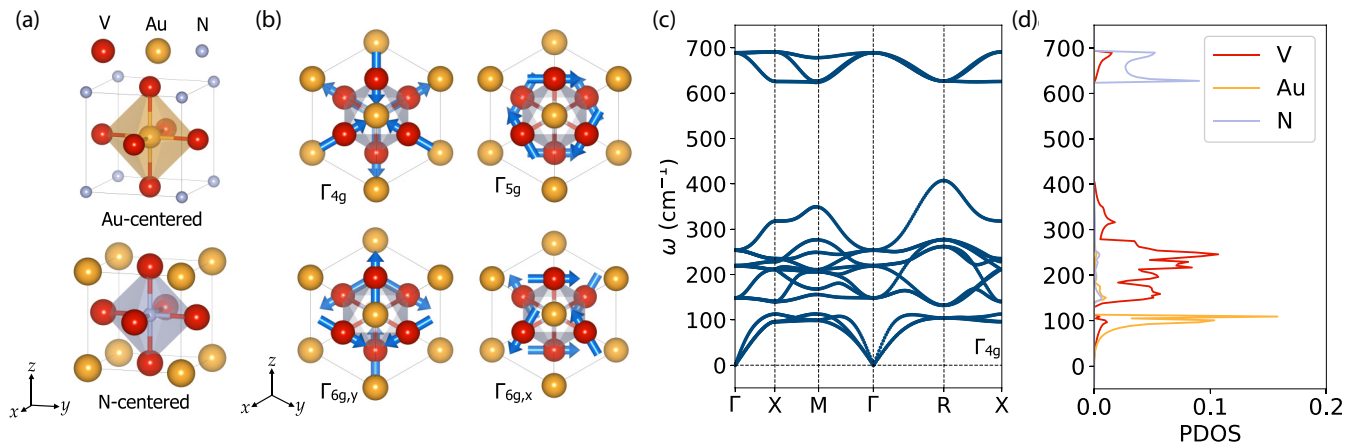


FIG. 1. (a)  $V_3AuN$   $Pm\bar{3}m$  structure for Au- and N-centered octahedra. (b)  $\Gamma_{4g}$ ,  $\Gamma_{5g}$ ,  $\Gamma_{6g,y}$ , and  $\Gamma_{6g,x}$  noncollinear magnetic orderings allowed in the antiperovskite with the crystallographic  $Pm\bar{3}m$  symmetry and labeled in agreement with Bertaut's notation [5,24]. (c) Full phonon-dispersion curves were computed at the N-centered antiperovskite considering  $\Gamma_{4g}$  noncollinear ordering along the  $\Gamma$ -X-M- $\Gamma$ -R-X path in the Brillouin zone. (d) Projected phonon DOS for the V, Au, and N sites. Here, a fully stable structure can be appreciated for this magnetic solution.

with  $A = Ni, Sn, Ge, Ga,$  and  $Pt$ . Moreover, our results show that in the Au-centered antiperovskite the relaxed lattice parameter is  $a = 5.029 \text{ \AA}$ , far from the experimentally reported value of  $a = 3.962 \text{ \AA}$ . Thus, as indicated by our results and by Rieger *et al.* [32], such an Au-centered structure is considerably higher in energy, and the N-centered structure is potentially the crystallographic ground state. As observed in the  $Mn_3NiN$  antiperovskite, it is recommended to correct the electronic exchange correlation by including the Coulomb  $U$  repulsion parameter in the magnetically active cation to adequately reproduce the vibrational, structural, and electronic degrees of freedom in the  $V_3AuN$  [6,52]. Along these lines, we have fully relaxed the electronic and atomic structure of the  $V_3AuN$  compound within the metaGGA SCAN-based exchange correlation [34] and we obtained a relaxed lattice parameter of  $3.961 \text{ \AA}$  in good agreement with the experimentally reported value of  $a = 3.962 \text{ \AA}$  [32]. A  $U$  value within the PBEsol +  $U$  scheme was selected to reasonably reproduce the compound's lattice parameter and electronic features, as shown in Fig. S1 in the Supplemental Material [35]. Based on this criterion, we selected a  $U = 1.2 \text{ eV}$  in the magnetically active  $3d:V$  orbitals, which has been used in our calculations. Regarding the magnetic moment per vanadium atom, we obtained values of  $m = 1.134 \mu_B \text{ atom}^{-1}$  and  $m = 1.256 \mu_B \text{ atom}^{-1}$  for the PBEsol +  $U$  and SCAN exchange-correlation representations, respectively. We have also compared with calculations obtained by using hybrid functionals within the HSE06 scheme and found that, at the experimentally observed lattice parameter, the magnetic moment was  $m = 1.824 \mu_B \text{ atom}^{-1}$ . Despite the latter magnetic moment being larger than the one computed with the SCAN and PBEsol +  $U$  schemes, all of this confirms the magnetically active behavior of the  $V_3AuN$  antiperovskite, and further experimentally focused efforts are needed to confirm this observable.

Now, we describe the relationship between the ionic radius and the appearance of the antiperovskite and anti-postperovskite structures in the vanadium-based family. In the  $V_3AN$  group of compounds, most of the reported materials are

found to crystallize in the layered anti-postperovskite  $Cmcm$  structure that was also observed in the perovskite fluoride [17–19] and oxide [54–56] compounds. We also explored the possibility for the  $V_3AuN$  compound to crystallize in the  $Cmcm$  symmetry group. In Table I we show the calculated total energy values, per formula unit in  $\text{eV f.u.}^{-1}$ , as well as the relative energy differences in the  $V_3AN$  with  $A = P, As, Sb,$  and  $Au$ . The total energies were obtained after full electronic and atomic relaxation at the cubic antiperovskite  $Pm\bar{3}m$  and the anti-postperovskite  $Cmcm$  symmetries. As can be observed, the energy difference is quite significant, close to  $\Delta E = 1.576 \text{ eV}$ , for  $A = P$ . Thus, as soon as the corner site's atomic radius is increased, the energy difference is reduced when going from P to Sb, suggesting a possible condensation of the antiperovskite into cubic symmetry. Once we reach the  $A = Au$ , the energy difference is  $\Delta E = -0.189 \text{ eV}$  confirming the existence of the  $Pm\bar{3}m$  phase as the ground state over the layered  $Cmcm$ . Then, the lowest-energy structure of the compounds, except for  $A = Au$ , belongs to the  $Cmcm$  anti-postperovskite. In perovskites, this phase is a result, in most cases, of an increase in octahedral rotations and tilts

TABLE I. Total energy per formula unit, in  $\text{eV f.u.}^{-1}$ , computed for the antiperovskite  $Pm\bar{3}m$  and the anti-postperovskite  $Cmcm$  structures within the  $V_3AN$  family, with  $A = P, As, Sb,$  and  $Au$ . Here, a  $U = 1.2 \text{ eV}$  is considered for the V site. Total energy values are organized following the atomic radius of the A site,  $r_A$  in pm, also presented. The energy difference is taken as  $\Delta E = E_{Pm\bar{3}m} - E_{Cmcm}$ , also in  $\text{eV f.u.}^{-1}$ . Goldschmidt's tolerance factor  $t$  [53] was calculated considering the atomic radius as reported by Clementi *et al.* with  $r_V = 171 \text{ pm}$  and  $r_N = 56 \text{ pm}$  [21].

Compound	$Cmcm$	$Pm\bar{3}m$	$\Delta E$	$r_A$	$t$ factor
$V_3PN$	-44.237	-42.660	+1.576	98	0.84
$V_3AsN$	-42.578	-41.729	+0.849	114	0.89
$V_3SbN^a$	-40.917	-40.816	+0.100	133	0.95
$V_3AuN$	-40.728	-40.917	-0.189	174	1.07

<sup>a</sup>A = Sb compound is included for comparison.

induced by isotropic pressure applied to the orthorhombic  $Pnma$  phase. Consequently, when the rotations overpass a limit, close to  $26^\circ$ , the corner-shared octahedral lattice is broken and, to minimize the enthalpy, it converges to an edge-shared octahedra structure in which the octahedral layers are separated by  $A$ -site layers [57]. In other compounds, such as  $\text{CaIrO}_3$  where the  $A$ -site radius is small when compared to the octahedra formed by  $\text{IrO}_6$ , the structure crystallizes at atmospheric pressure in the  $Cmcm$  postperovskite symmetry [58,59], as in the  $\text{V}_3\text{PN}$  and  $\text{V}_3\text{AsN}$  cases. Therefore, in the anti-postperovskite structure, these results can be correlated with the corner site size, also presented in Table I, for which more significant is the  $A$  site, more minor is the octahedral free space, and smaller is the tendency to observe octahedral rotations and tiltings in the antiperovskite structure. The latter explains the cubic  $Pm\bar{3}m$  phase ground state rather than the  $Cmcm$  layered structure in the  $\text{V}_3\text{AuN}$  antiperovskite. In conclusion, the anti-postperovskite phase existence in the  $\text{V}_3\text{AN}$ ,  $A = \text{P, As, and Sb}$ , is explained in terms of the tolerance factor in the perovskite structure (see Table I). Then, as soon as the  $A$  site becomes smaller, more significant octahedral  $\text{NV}_6$  rotations are expected up to the point where the crystal cannot hold the corner-shared structure, and then, a reorganization into the layered structure is expected. Consequently, large  $A$  sites in the  $\text{V}_3\text{AN}$  should be explored to stabilize and favor the cubic corner-shared structure. Table I includes the  $t$  Goldschmidt's tolerance factor [53] computed by considering the atomic radius as reported by Clementi *et al.* [21]. Here, the  $t = (r_A + r_V)/[\sqrt{2}(r_N + r_V)]$ , where  $r_V$ ,  $r_N$ , and  $r_A$  are the atomic radius of the vanadium, nitrogen, and the considered  $A$  sites, respectively. This parameter has been useful in the characterization and identification of the possible distortive, group-to-subgroup, phase transitions expected in perovskite-like compounds based on geometrical considerations. When  $t < 0.7$ , large octahedral rotations are expected to break the corner-shared structure and, for example, trigonal structures are observed. For  $t$  values between 0.7 to 0.9, orthorhombic and/or rhombohedral symmetries can be expected. For values between 0.9 to 1.0, a complete removal of the octahedral distortions and tiltings can be observed and consequently, cubic symmetries are foreseen. Finally, at values  $t > 1$ , hexagonal phases have been demonstrated where the corner-shared octahedral lattice is broken again. As can be noted from the  $t$  values across the entire  $\text{V}_3\text{AN}$  family, for  $A = \text{P, As, and Sb}$ , the  $t$  value is smaller than 1 in agreement with the expected rotations and post-antiperovskite phase transition. As such, for the  $A = \text{Au}$ , the cubic symmetry is observed as the  $t$  value is close to 1.

Once we have understood the crystallographic degrees of freedom, we explore the electronic and the allowed noncollinear magnetic structures. To do so, we examined the symmetry-allowed magnetic orderings, with a propagation vector  $\mathbf{q} = (0, 0, 0)$ , in the  $\text{V}_3\text{AuN}$  antiperovskite. This structure allows four different noncollinear magnetic orderings, resulting from the relaxation of magnetic frustration expected in the kagome lattices. The latter are formed by vanadium sites in the  $\langle 111 \rangle$  family of planes. In Fig. 1(b) are shown the  $\Gamma_{4g}$ ,  $\Gamma_{5g}$ ,  $\Gamma_{6g,y}$ , and  $\Gamma_{6g,x}$  magnetic orderings that reduce the  $Pm\bar{3}m$  crystallographic symmetry group to the  $R\bar{3}m'$  (MSG 166.101),  $R\bar{3}m$  (MSG 166.97),  $C2'/m'$  (MSG 12.62), and  $C2/m$  (MSG

12.58) magnetic symmetry groups, respectively. In the  $\langle 111 \rangle$  plane, these orderings hold a magnetic moment vector chirality of  $+1$  in the  $\Gamma_{4g}$  and  $\Gamma_{5g}$  whereas it is  $-1$  in the  $\Gamma_{6g,y}$  and  $\Gamma_{6g,x}$  [60,61]. It is worth mentioning that the magnetic vector chirality is defined as  $\kappa = \frac{2}{3\sqrt{3}} \sum_{i,j} (\mathbf{S}_i \times \mathbf{S}_j) = \frac{2}{3\sqrt{3}} (\mathbf{S}_1 \times \mathbf{S}_2 + \mathbf{S}_2 \times \mathbf{S}_3 + \mathbf{S}_3 \times \mathbf{S}_1)$  for the kagome lattice where the  $i$  and  $j$  indexes run over the magnetic moments in the unit cell [62]. The latter moments per V site are shown in Table SI in the Supplemental Material for each of the noncollinear antiferromagnetic orderings [35]. Thus, the  $+1$  and  $-1$  refer to the magnetic chiral vector pointing along the  $[111]$  and  $[\bar{1}\bar{1}\bar{1}]$ , respectively, and with a magnitude close to 1. After a complete electronic and atomic relaxation within the four noncollinear antiferromagnetic states, we obtained a total energy per formula unit of  $-41.4020$  eV f.u. $^{-1}$ ,  $-41.4011$  eV f.u. $^{-1}$ ,  $-41.4012$  eV f.u. $^{-1}$ , and  $-41.4015$  eV f.u. $^{-1}$  for the  $\Gamma_{4g}$ ,  $\Gamma_{5g}$ ,  $\Gamma_{6g,y}$ , and  $\Gamma_{6g,x}$  orderings, respectively. For comparison, we also relaxed the FM state,  $R\bar{3}m'$  (MSG 166.101), with the magnetic moments pointing toward the  $\langle 111 \rangle$  axis. We obtained a total energy of  $-41.3066$  eV f.u. $^{-1}$  in this magnetic state. Thus, we estimated the energy differences with reference to the FM ordering and obtained that  $\Delta E = -95.4$  meV f.u. $^{-1}$ ,  $-94.5$  meV f.u. $^{-1}$ ,  $-94.6$  meV f.u. $^{-1}$ , and  $-94.9$  meV f.u. $^{-1}$  for the  $\Gamma_{4g}$ ,  $\Gamma_{5g}$ ,  $\Gamma_{6g,y}$ , and  $\Gamma_{6g,x}$  orderings, respectively. As such, in terms of the magnetocrystalline anisotropic energy, the  $\text{V}_3\text{AuN}$  prefers a noncollinear antiferromagnetic solution as expected from the triangular coordination in the kagome lattice and magnetic frustration of the V sites. The minor differences in the energy, less than 1 meV between antiferromagnetic orderings, suggest that these magnetic states barely degenerate, and they might be observed experimentally with a preference for the  $\Gamma_{4g}$  order.

Aiming to explore the lattice dynamics and to confirm the vibrational stability of the  $\text{V}_3\text{AuN}$  compound in the cubic antiperovskite symmetry within the noncollinear magnetic orderings, we computed the phonon-dispersion curves by considering the four chiral noncollinear antiferromagnetic states. These calculations were performed following the procedure based on the finite-displacement method [39,40]. Here, we use a  $2 \times 2 \times 2$  supercell in which the noncollinear chiral antiferromagnetic ordering is preserved, and the displacements are considered within the  $R\bar{3}m$  crystallographic symmetry. Later, the dynamical matrix is reconstructed and the phonon-dispersion curves are extracted. This methodology was also used for the  $\text{Mn}_3\text{NiN}$  antiperovskite in which a large magnetostructural coupling is observed [6]. In Fig. 1(c), we present the full phonon-dispersion curves for the ground state  $\Gamma_{4g}$ , along the cubic symmetry path reference for simplicity. The vibrational landscape demonstrates that the N-centered cubic antiperovskite is fully stable with no negative phonons (i.e., unstable modes) in the  $\Gamma_{4g}$  ground state. Regarding the other three antiferromagnetic orderings, the phonon dispersion curves also show fully dynamically stable structures as shown in Fig. S2 in the Supplemental Material, with no major difference for those antiferromagnetic orderings [35]. In Fig. 1(d) is presented the projected phonon DOS extracted for the  $\Gamma_{4g}$  order. As can be observed, the phonons around  $100$   $\text{cm}^{-1}$  are strongly dominated by Au sites with a slight overlap with the V sites because of the small

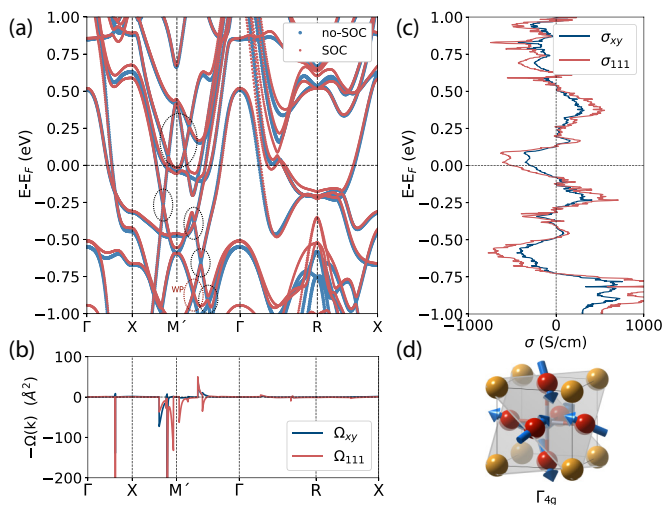


FIG. 2. (a) Electronic bands computed for the  $\Gamma_{4g}$  ordering in the  $V_3AuN$  along the  $\Gamma$ - $X$ - $M'$ - $\Gamma$ - $R$ - $X$  path in the Brillouin zone, with and without spin-orbit coupling. In the dashed black ovals are marked the band's crossing nodes that are gapped once the SOC is included. In the red oval is marked the symmetry-protected Weyl crossing along the  $M'$ - $\Gamma$  path. In (b) we present the computed Berry curvature,  $\Omega_{xy}(\mathbf{k})$  and  $\Omega_{111}(\mathbf{k})$ , along the same  $k$  path selected for the electronic bands. (c) Anomalous Hall conductivity,  $\sigma_{xy}$  and  $\sigma_{111}$ , components were computed for the  $\Gamma_{4g}$  ordering. (d)  $\Gamma_{4g}$  magnetic state, in which the magnetic moments at the vanadium atoms are denoted by blue arrows.

contribution to Au-driven eigendisplacements. For frequencies between  $140 \text{ cm}^{-1}$  and  $400 \text{ cm}^{-1}$ , we observe the vibrational modes dominated by the V-site eigendisplacements. Such atomic vibrations are associated with octahedral rotations and tiltings related to the kagome lattice. Finally, the N site's phonons are located between  $600 \text{ cm}^{-1}$  and  $700 \text{ cm}^{-1}$ , well above large frequency values. We found a band gap in the phonon dispersion between acoustic and optical modes, located close to  $120 \text{ cm}^{-1}$ . The latter phononic band gap prevents the propagation of mechanical waves at a defined frequency range. This is importantly observed in phononic crystals [63,64] and 2D [65] and 3D monochalcogenides [66]. As such, the phononic band gap suggests the prohibited propagation frequencies between  $113 \text{ cm}^{-1}$  and  $140 \text{ cm}^{-1}$ , taken at the X point in the BZ and potentially affecting the thermal properties, such as thermal conductivity, among others. This band gap can be potentially attributed to the significantly different eigendisplacements below the band gap, driven by antipolar displacements of the Au site along the  $z$  axis and above, dominated by the motion of the  $NV_6$  octahedral in the  $xy$  plane. The latter is enhanced by the large mass difference between the Au sites,  $w_{Au} = 196.9665 \text{ amu}$ , and the V and N sites with  $w_V = 50.9415 \text{ amu}$  and  $w_N = 14.0067 \text{ amu}$ , respectively, as suggested by Argaman *et al.* [66]. Nonetheless, the specific details of the physical source of the phononic band gap, and its potential influence on the thermodynamical observables, are to be studied in further work.

Moving forward, in Fig. 2(a), we present the computed electronic band structure across the high-symmetry points of the cubic reference for the  $\Gamma_{4g}$  state with and without the

effect of the spin-orbit coupling, SOC. Here, we observe the expected metallic behavior with a predominant contribution from the V sites close to the Fermi energy. In the path along  $X$ - $M'$ - $\Gamma$  high-symmetry points, we observed linear band crossings associated with nodal points in proximity to the Fermi level without SOC. After the spin-orbit coupling is considered, most of nodes are gapped, as marked in the black ovals. The latter has been also observed, for example, in  $Cs_2LiMn_3F_{12}$  [67], TaAs [68], and  $Fe_3Sn_2$  [69] and explained in terms of the strongly correlated magnetism, topological features, and symmetry consideration entanglement that induces massive fermions. In Fig. 2(a) we observe a fully protected Weyl point between the  $\Gamma$ - $M'$  path at the  $(0.36, 0.00, -0.36)$   $k$  point and  $E = -0.872 \text{ eV}$ , marked by the red oval. It is worth mentioning that the  $M'$  point is located at the  $(0.5, 0.0, -0.5)$  instead of the  $(0.5, 0.5, 0.0)$  regular  $M$  point. This choice is taken due to the magnetic symmetries that are strongly entangled with the topological properties in the  $V_3AuN$  [12,70]. The  $M'$  is located within the magnetic kagome lattice, at the  $(111)$  plane, and it is conserved by the  $\{\bar{1}10\}$  mirror plane. To better portray the importance of the crystallographic and magnetic symmetry conditions, in Fig. S3 we included the band structure for the  $\Gamma$ - $M$  and  $\Gamma$ - $M'$  paths. As commented on before, the Weyl crossing appears gapped due to the symmetry conditions considering that the  $M$  point is out of the  $(111)$  magnetic kagome lattice plane and not protected by the  $\{\bar{1}10\}$ , in contrast to the path running toward  $M'$ . Afterward, and considering the magnetic symmetry groups, we observe that the ground state antiferromagnetic  $\Gamma_{4g}$  ordering allows for the appearance of nonzero Berry curvature and, therefore, net components of the anomalous Hall conductivity (AHC) tensor [71]. The latter is also allowed in the  $\Gamma_{6g,x}$  and  $\Gamma_{6g,y}$  magnetic orderings with different tensors [72]. As such, in Fig. 2(b) and in Fig. 2(c) are presented the Berry curvature,  $\Omega_{xy}(\mathbf{k})$  and  $\Omega_{111}(\mathbf{k})$ , and the anomalous Hall conductivity,  $\sigma_{xy}$  and  $\sigma_{111}$ , components, respectively. These were computed at the  $\Gamma_{4g}$  magnetic ordering ground state, also included in Fig. 2(d). The Berry curvature and AHC components within the  $[111]$  plane were computed such as  $\Omega_{111}(\mathbf{k}) \equiv \frac{1}{\sqrt{3}}[\Omega_{xy}(\mathbf{k}) + \Omega_{yz}(\mathbf{k}) + \Omega_{zx}(\mathbf{k})]$  and  $\sigma_{111} \equiv \frac{1}{\sqrt{3}}(\sigma_{xy} + \sigma_{yz} + \sigma_{zx})$ , respectively. We observed that the  $\Omega_{111}(\mathbf{k})$  component, as well as the  $\Omega_{xy}(\mathbf{k})$ , have considerable net values along the  $\Gamma$ - $X$ ,  $X$ - $M$ , and  $\Gamma$ - $M'$  paths with divergent behavior in the  $\Gamma$ - $X$ ,  $X$ - $M'$ . Importantly, although the Weyl points are allowed by symmetry in the antiferromagnetic antiperovskites [50], our results suggest that the major contribution to the  $\Omega_{xy}(\mathbf{k})$ , and consequently to  $\sigma_{xy}$ , is related to the presence of prevented band crossings and band decoherence induced by the spin-orbit coupling effect, close to the Fermi energy. This can be observed by correlating the band structure and the  $\Omega_{xy}(\mathbf{k})$ , in Figs. 2(a) and 2(b), along the shown  $k$  path. The latter observation is in agreement with recent findings in the  $Mn_3NiN$  antiperovskite compound [52] where the strain tuning of the AHC reveals that the Weyl node contribution is canceled out over the entire BZ [73]. After calculating the  $\sigma_{xy}$  ( $\sigma_{111}$ ) component at the Fermi energy, we obtained a value of  $\sigma_{xy} = -291 \text{ S cm}^{-1}$  ( $\sigma_{111} = -504 \text{ S cm}^{-1}$ ). This AHC value obtained in the  $V_3AuN$  is, to date, among the largest observed

in the antiferromagnetic antiperovskite family. This considerable value is explained in terms of the large spin-orbit coupling of the Au sites transferred to the kagome lattice through hybridization with V sites [20]. Here, it is important to mention that according to Huyen *et al.* [50], the largest theoretically reported AHC value has been calculated in the  $\text{Mn}_3\text{PtN}$  antiperovskite with  $\sigma_{xy} = 462 \text{ S cm}^{-1}$  ( $\sigma_{111} = 800 \text{ S cm}^{-1}$ ) [50]; nevertheless, in our calculations we obtained an  $E_{MAE} = E_{\Gamma_{4g}} - E_{\Gamma_{5g}} = 1.9 \text{ meV}$  for the  $\text{Mn}_3\text{PtN}$  compound. This suggests the  $\Gamma_{5g}$  as the magnetic ground state in which the AHC is forbidden by symmetry. This finding also agrees with the results of Singh *et al.* [14]. Furthermore, at this point, it is worth commenting that in most of the reported literature, the calculations have been performed within the PBE approach, and no Hubbard term has been considered; therefore, no electronic correction has been explored, aiming to remove the computational chemical pressure and to obtain fully relaxed lattice parameters [50,51,74,75]. Thus, the exchange-correlation energy, which strongly influences the magnetic and electronic structure, has not been included considering the Coulomb repulsion value  $U$ , which, based on our analysis, tends to considerably reduce the band spreading and, therefore, affects the electronic structure close to the Fermi level and reduces the computed AHC values [6,52]. Moreover, this exchange-correlation correction affects the structural parameters where the experimentally observed lattice parameter can be obtained after carefully introducing the PBEsol +  $U$  methodology, as discussed above. After including the value of  $U = 2.0 \text{ eV}$  in the  $3d:\text{Mn}$  orbitals for the  $\text{Mn}_3\text{PtN}$  compound, fitted to reproduce the experimentally obtained lattice parameter within the PBEsol +  $U$  scheme, we found that  $\sigma_{xy} = 144 \text{ S cm}^{-1}$  ( $\sigma_{111} = 249 \text{ S cm}^{-1}$ ) in the  $\Gamma_{4g}$  higher in energy and metastable magnetic ordering. Evidently, this value is considerably smaller than the reported one. For example, in the  $\text{Mn}_3\text{NiN}$  case, Torres-Amaris *et al.* [52] showed that under the PBEsol +  $U$  scheme, as shown here, the AHC is  $\sigma_{xy} = 68 \text{ S cm}^{-1}$ , in better agreement with the experimentally reported value of  $\sigma_{xy} = 22 \text{ S cm}^{-1}$  in thin films [74], and considerably smaller than the calculated value of  $\sigma_{xy} = 130\text{--}170 \text{ S cm}^{-1}$  in Refs. [74,75] where no correction was considered. In the  $\text{V}_3\text{AuN}$  antiperovskite case,  $\sigma_{xy} = -361 \text{ S cm}^{-1}$  ( $\sigma_{111} = -623 \text{ S cm}^{-1}$ ) with the smallest  $U$  value (i.e.,  $U = 0.4 \text{ eV}$ ) that reproduce the magnetic response and symmetry operations; see Fig. S1. These variations in the AHC components suggest the importance of the  $U$  value in the electronic properties in this type of antiperovskite compound. Furthermore, the PBEsol failure to reproduce the experimental lattice parameter is solved by including  $U$  to correctly produce the spin-phonon coupling in these antiperovskites. The validation with the metaGGA SCAN calculations indicates that the exchange correlation needs to be treated carefully in this type of material. As such, we have also computed the AHC component within the SCAN formalism in the  $\text{V}_3\text{AuN}$  antiperovskite and we found that  $\sigma_{xy} = -347 \text{ S cm}^{-1}$  ( $\sigma_{111} = -600 \text{ S cm}^{-1}$ ), in fair agreement with the values obtained by the PBEsol +  $U$  approach. Furthermore, it is worth commenting that SCAN-based calculations have also shown a considerable improvement in describing the electronic and structural behavior in Mn-rich compounds [76], Heusler alloys [77], metal oxides

[78], and in the  $\text{Mn}_3\text{NiN}$  antiperovskite [6], even though several reports suggest an overestimation of the magnetic moment when the exchange-correlation SCAN is used. In the case of antiperovskites, the total magnetic moment is zero due to the antiferromagnetic ordering ground state. Moreover, there is no suggested connection between the magnetic moment per atom and the AHC, which here only depends on the symmetry operations associated with the overall antiferromagnetic noncollinear ordering. Therefore, a future detailed work dedicated to exploring the dependence of the electronic and magnetic structure on the exchange-correlation approach in these and other magnetically driven topological materials is highly desirable. Notably, although the antiferromagnetic chiral structure is responsible for the symmetry conditions that allow the appearance of net Berry curvature and topological features, the allocation of  $5d$  heavy atoms in the lattice, such as Au in this case, considerably enhances the AHC values due to their sizable spin-orbit coupling when compared to  $4d$  and  $3d$  metals [14,20,50]. Finally, we believe that our work opens the possibility for the existence of other antiperovskite compounds, such as  $\text{V}_3\text{AgN}$  and  $\text{V}_3\text{BiN}$ , where the Bi's and Ag's large atomic size could induce an N-centered cubic antiperovskite structure, in addition to the expected sizable spin-orbit coupling interaction that can give rise to large AHC and unexpected properties associated with their topological features. Our results show that closed-shell elements, such as  $A = \text{Ag}$  and  $\text{Bi}$ , retain the magnetism in the  $\text{V}_3\text{AN}$  compounds, whereas open-shell cations, such as  $A = \text{Pt}$  and  $\text{Ir}$ , induce a nonmagnetic state. This observation calls attention to further studies aiming to investigate in more detail the effect of the  $A$  site on the electronic properties among all the antiperovskite compounds.

#### IV. CONCLUSIONS

We have investigated, using first-principles calculations, the vanadium-based antiperovskite nitride  $\text{V}_3\text{AuN}$ . Despite the reported Au-centered octahedral antiperovskite structure, the N-centered structure is potentially the ground state energy structure. It is supported by the fact that it is also dynamically stable, as demonstrated by the computed phonon-dispersion curves. Additionally, the  $\text{V}_3\text{AuN}$  is the first reported vanadium-based antiperovskite that belongs to cubic symmetry rather than the layered post-antiperovskite materials reported among the  $\text{V}_3\text{AN}$  family. The cubic structure entirely agrees with other Mn- and Cr-based antiperovskites compounds. As observed, four different noncollinear magnetic orderings are allowed resulting from the magnetic frustration in the kagome lattices formed by the vanadium sites in the  $\langle 111 \rangle$  family of planes. Here, we observed that the chiral  $\Gamma_{4g}$  is the lowest-energy magnetic ground state in which a nonzero Berry curvature and, consequently, a tangible anomalous Hall conductivity is present. Interestingly, when the exchange-correlation correction is considered, and the correct magnetic ground state is taken into account in the  $\text{Mn}_3\text{PtN}$  compound, the computed  $\sigma_{xy}$  and  $\sigma_{111}$  values in the  $\text{V}_3\text{AuN}$  are among the largest reported in the antiperovskite family of materials, of course, waiting for experimental confirmation. Finally, we hope our results will motivate more studies in these novel antiferromagnetic antiperovskite families of

materials. Those with several topological signatures that couple to the fascinating magnetic response can be explored and possibly controlled for future antiperovskite spin-based devices.

### ACKNOWLEDGMENTS

Calculations presented in this article were carried out using the GridUIS-2 experimental test bed. The latter was developed under the Universidad Industrial de Santander (SC3-UIS) High Performance and Scientific Computing Centre with support from UIS Vicerrectoría de Investigación y Extensión

(VIE-UIS) and several UIS research groups. We also acknowledge the computational resources awarded by XSEDE, a project supported by National Science Foundation, Grant No. ACI-1053575. The authors also acknowledge support from the Texas Advanced Computer Center (with the Stampede2 and Bridges supercomputers). Additionally, we also recognize the supercomputing system Thorny Flat at WVU, which is partially funded by the National Science Foundation (NSF) Major Research Instrumentation Program (MRI), Award No. 1726534, and West Virginia University. A.C.G.C. acknowledge Grant No. 2677 entitled “Quiralidad y Ordenamiento Magnético en Sistemas Cristalinos: Estudio Teórico desde Primeros Principios” supported by the VIE-UIS.

- 
- [1] Y. Wang, H. Zhang, J. Zhu, X. Lü, S. Li, R. Zou, and Y. Zhao, Antiperovskites with exceptional functionalities, *Adv. Mater.* **32**, 1905007 (2019).
- [2] A. C. Garcia-Castro, R. Ospina, and J. H. Quintero, Octahedral distortion and electronic properties of the antiperovskite oxide  $\text{Ba}_3\text{SiO}$ : First principles study, *J. Phys. Chem. Solids* **136**, 109126 (2020).
- [3] A. C. Garcia-Castro, J. H. Quintero Orozco, and C. J. Paez Gonzalez, Hybrid-improper ferroelectric behavior in  $\text{Ba}_3\text{SiO}/\text{Ba}_3\text{GeO}$  oxide antiperovskite superlattices, *Eur. Phys. J. B* **92**, 203 (2019).
- [4] M. Wu, C. Wang, Y. Sun, L. Chu, J. Yan, D. Chen, Q. Huang, and J. W. Lynn, Magnetic structure and lattice contraction in  $\text{Mn}_3\text{NiN}$ , *J. Appl. Phys.* **114**, 123902 (2013).
- [5] D. Fruchart and E. F. Bertaut, Magnetic studies of the metallic perovskite-type compounds of manganese, *J. Phys. Soc. Jpn.* **44**, 781 (1978).
- [6] L. Flórez-Gómez, W. Ibarra-Hernández, and A. Garcia-Castro, Lattice dynamics and spin-phonon coupling in the noncollinear antiferromagnetic antiperovskite  $\text{Mn}_3\text{NiN}$ , *J. Magn. Magn. Mater.* **562**, 169813 (2022).
- [7] D. Boldrin, E. Mendive-Tapia, J. Zemen, J. B. Staunton, T. Hansen, A. Aznar, J.-L. Tamarit, M. Barrio, P. Lloveras, J. Kim, X. Moya, and L. F. Cohen, Multisite Exchange-Enhanced Barocaloric Response in  $\text{Mn}_3\text{NiN}$ , *Phys. Rev. X* **8**, 041035 (2018).
- [8] D. Boldrin, F. Johnson, R. Thompson, A. P. Mihai, B. Zou, J. Zemen, J. Griffiths, P. Gubelj, K. L. Ormandy, P. Manuel, D. D. Khalyavin, B. Ouladdiaf, N. Qureshi, P. Petrov, W. Branford, and L. F. Cohen, The biaxial strain dependence of magnetic order in spin frustrated  $\text{Mn}_3\text{NiN}$  thin films, *Adv. Funct. Mater.* **29**, 1902502 (2019).
- [9] P. Lukashev, R. F. Sabirianov, and K. Belashchenko, Theory of the piezomagnetic effect in mn-based antiperovskites, *Phys. Rev. B* **78**, 184414 (2008).
- [10] J. Zemen, Z. Geraci, and K. G. Sandeman, Piezomagnetism as a counterpart of the magnetovolume effect in magnetically frustrated Mn-based antiperovskite nitrides, *Phys. Rev. B* **96**, 024451 (2017).
- [11] E. V. Gomonaj, Magnetostriction and piezomagnetism of non-collinear antiferromagnet  $\text{Mn}_3\text{NiN}$ , *Phase Transitions* **18**, 93 (1989).
- [12] E. Liu, Y. Sun, N. Kumar, L. Muechler, A. Sun, L. Jiao, S. Y. Yang, D. Liu, A. Liang, Q. Xu, J. Kroder, V. Süß, H. Borrmann, C. Shekhar, Z. Wang, C. Xi, W. Wang, W. Schnelle, S. Wirth, Y. Chen *et al.*, Giant anomalous Hall effect in a ferromagnetic kagome-lattice semimetal, *Nat. Phys.* **14**, 1125 (2018).
- [13] H. Tsai, T. Higo, K. Kondou, T. Nomoto, A. Sakai, A. Kobayashi, T. Nakano, K. Yakushiji, R. Arita, S. Miwa, Y. Otani, and S. Nakatsuji, Electrical manipulation of a topological antiferromagnetic state, *Nature (London)* **580**, 608 (2020).
- [14] H. K. Singh, I. Samathrakris, N. M. Fortunato, J. Zemen, C. Shen, O. Gutfleisch, and H. Zhang, Multifunctional antiperovskites driven by strong magnetostructural coupling, *npj Comput. Mater.* **7**, 98 (2021).
- [15] B. Wang and K. Ohgushi, Superconductivity in anti-post-perovskite vanadium compounds, *Sci. Rep.* **3**, 3381 (2013).
- [16] A. R. Oganov and S. Ono, Theoretical and experimental evidence for a post-perovskite phase of  $\text{MgSiO}_3$  in Earth’s  $D''$  layer, *Nature (London)* **430**, 445 (2004).
- [17] A. C. Garcia-Castro, A. H. Romero, and E. Bousquet, Non-collinear magnetism in post-perovskites from first principles: Comparison between  $\text{CaRhO}_3$  and  $\text{NaNiF}_3$ , *Phys. Status Solidi B* **252**, 689 (2015).
- [18] H. Yusa, Y. Shirako, M. Akaogi, H. Kojitani, N. Hirao, Y. Ohishi, and T. Kikegawa, Perovskite-to-postperovskite transitions in  $\text{NaNiF}_3$  and  $\text{NaCoF}_3$  and disproportionation of  $\text{NaCoF}_3$  postperovskite under high pressure and high temperature, *Inorg. Chem.* **51**, 6559 (2012).
- [19] A. C. Garcia-Castro, A. H. Romero, and E. Bousquet, First-principles study of vibrational and noncollinear magnetic properties of the perovskite to postperovskite pressure transition of  $\text{NaNiF}_3$ , *Phys. Rev. B* **90**, 064113 (2014).
- [20] H. Chen, Q. Niu, and A. H. MacDonald, Anomalous Hall Effect Arising from Noncollinear Antiferromagnetism, *Phys. Rev. Lett.* **112**, 017205 (2014).
- [21] E. Clementi, D. L. Raimondi, and W. P. Reinhardt, Atomic screening constants from SCF functions. II. Atoms with 37 to 86 electrons, *J. Chem. Phys.* **47**, 1300 (1967).
- [22] P. X. Qin, H. Yan, X. N. Wang, Z. X. Feng, H. X. Guo, X. R. Zhou, H. J. Wu, X. Zhang, Z. G. G. Leng, H. Y. Chen, and Z. Q. Liu, Noncollinear spintronics and electric-field control: A review, *Rare Metals* **39**, 95 (2020).

- [23] G. Gurung, D.-F. Shao, and E. Y. Tsymbal, Spin-torque switching of noncollinear antiferromagnetic antiperovskites, *Phys. Rev. B* **101**, 140405(R) (2020).
- [24] J.-R. Soh, F. de Juan, N. Qureshi, H. Jacobsen, H.-Y. Wang, Y.-F. Guo, and A. T. Boothroyd, Ground-state magnetic structure of  $\text{Mn}_3\text{Ge}$ , *Phys. Rev. B* **101**, 140411(R) (2020).
- [25] P. Hohenberg and W. Kohn, Inhomogeneous electron gas, *Phys. Rev.* **136**, B864 (1964).
- [26] W. Kohn and L. J. Sham, Self-consistent equations including exchange and correlation effects, *Phys. Rev.* **140**, A1133 (1965).
- [27] G. Kresse and J. Furthmüller, Efficient iterative schemes for *ab initio* total-energy calculations using a plane-wave basis set, *Phys. Rev. B* **54**, 11169 (1996).
- [28] G. Kresse and D. Joubert, From ultrasoft pseudopotentials to the projector augmented-wave method, *Phys. Rev. B* **59**, 1758 (1999).
- [29] P. E. Blöchl, Projector augmented-wave method, *Phys. Rev. B* **50**, 17953 (1994).
- [30] J. P. Perdew, A. Ruzsinszky, G. I. Csonka, O. A. Vydrov, G. E. Scuseria, L. A. Constantin, X. Zhou, and K. Burke, Restoring the Density-Gradient Expansion for Exchange in Solids and Surfaces, *Phys. Rev. Lett.* **100**, 136406 (2008).
- [31] A. I. Liechtenstein, V. I. Anisimov, and J. Zaanen, Density-functional theory and strong interactions: Orbital ordering in Mott-Hubbard insulators, *Phys. Rev. B* **52**, R5467(R) (1995).
- [32] W. Rieger, H. Nowotny, and F. Benesovsky, Phasen mit oktaedrischen bauelementen des übergangsmetalls, *Monatshefte für Chemie und verwandte Teile anderer Wissenschaften* **96**, 232 (1965).
- [33] J. Sun, M. Marsman, G. I. Csonka, A. Ruzsinszky, P. Hao, Y.-S. Kim, G. Kresse, and J. P. Perdew, Self-consistent meta-generalized gradient approximation within the projector-augmented-wave method, *Phys. Rev. B* **84**, 035117 (2011).
- [34] J. Sun, A. Ruzsinszky, and J. P. Perdew, Strongly Constrained and Appropriately Normed Semilocal Density Functional, *Phys. Rev. Lett.* **115**, 036402 (2015).
- [35] See Supplemental Material at <http://link.aps.org/supplemental/10.1103/PhysRevMaterials.6.125003> for detailed information on the Coulomb  $U$  correction in the exchange-correlation representation; full phonon-dispersion curves for the chiral  $\Gamma_{5g}$ ,  $\Gamma_{6g,x}$ , and  $\Gamma_{6g,y}$  antiferromagnetic noncollinear orderings; a table containing the magnetic components for all the orderings; and finally, the electronic bands along the  $\Gamma$ -M and  $\Gamma$ -M' paths.
- [36] A. V. Krkavau, O. A. Vydrov, A. F. Izmaylov, and G. E. Scuseria, Influence of the exchange screening parameter on the performance of screened hybrid functionals, *J. Chem. Phys.* **125**, 224106 (2006).
- [37] H. J. Monkhorst and J. D. Pack, Special points for Brillouin-zone integrations, *Phys. Rev. B* **13**, 5188 (1976).
- [38] D. Hobbs, G. Kresse, and J. Hafner, Fully unconstrained noncollinear magnetism within the projector augmented-wave method, *Phys. Rev. B* **62**, 11556 (2000).
- [39] K. Kunc and R. M. Martin, *Ab Initio* Force Constants of GaAs: A New Approach to Calculation of Phonons and Dielectric Properties, *Phys. Rev. Lett.* **48**, 406 (1982).
- [40] P. K. Lam, M. M. Dacorogna, and M. L. Cohen, Self-consistent calculation of electron-phonon couplings, *Phys. Rev. B* **34**, 5065 (1986).
- [41] A. Togo and I. Tanaka, First principles phonon calculations in materials science, *Scr. Mater.* **108**, 1 (2015).
- [42] A. A. Mostofi, J. R. Yates, G. Pizzi, Y.-S. Lee, I. Souza, D. Vanderbilt, and N. Marzari, An updated version of Wannier90: A tool for obtaining maximally-localised Wannier functions, *Comput. Phys. Commun.* **185**, 2309 (2014).
- [43] G. Pizzi, V. Vitale, R. Arita, S. Blügel, F. Freimuth, G. Géranton, M. Gibertini, D. Gresch, C. Johnson, T. Koretsune, J. Ibañez-Azpiroz, H. Lee, J.-M. Lihm, D. Marchand, A. Marrazzo, Y. Mokrousov, J. I. Mustafa, Y. Nohara, Y. Nomura, L. Paulatto *et al.*, Wannier90 as a community code: New features and applications, *J. Phys.: Condens. Matter* **32**, 165902 (2020).
- [44] S. S. Tsirkin, High performance Wannier interpolation of Berry curvature and related quantities with WannierBerri code, *npj Comput. Mater.* **7**, 33 (2021).
- [45] K. Momma and F. Izumi, *VESTA3* for three-dimensional visualization of crystal, volumetric and morphology data, *J. Appl. Crystallogr.* **44**, 1272 (2011).
- [46] K. Persson, Materials data on  $\text{V}_3\text{AuN}$  (sg:221) by Materials Project, <https://materialsproject.org/materials/mp-635460>.
- [47] A. Jain, S. P. Ong, G. Hautier, W. Chen, W. D. Richards, S. Dacek, S. Cholia, D. Gunter, D. Skinner, G. Ceder, and K. Persson, The Materials Project: A materials genome approach to accelerating materials innovation, *APL Mater.* **1**, 011002 (2013).
- [48] G. Bergerhoff, R. Hundt, R. Sievers, and I. D. Brown, The inorganic crystal structure data base, *J. Chem. Inf. Comput. Sci.* **23**, 66 (1983).
- [49] A. Belsky, M. Hellenbrandt, V. L. Karen, and P. Luksch, New developments in the Inorganic Crystal Structure Database (ICSD): Accessibility in support of materials research and design, *Acta Crystallogr. Sect. B* **58**, 364 (2002).
- [50] V. T. N. Huyen, M.-T. Suzuki, K. Yamauchi, and T. Oguchi, Topology analysis for anomalous Hall effect in the noncollinear antiferromagnetic states of  $\text{Mn}_3\text{AN}$  (A = Ni, Cu, Zn, Ga, Ge, Pd, In, Sn, Ir, Pt), *Phys. Rev. B* **100**, 094426 (2019).
- [51] I. Opahle, H. K. Singh, J. Zemen, O. Gutfleisch, and H. Zhang, Effect of N, C, and B interstitials on the structural and magnetic properties of alloys with  $\text{Cu}_3\text{Au}$  structure, *Phys. Rev. Res.* **2**, 023134 (2020).
- [52] D. Torres-Amaris, A. Bautista-Hernandez, R. González-Hernández, A. H. Romero, and A. C. Garcia-Castro, Anomalous Hall conductivity control in  $\text{Mn}_3\text{NiN}$  antiperovskite by epitaxial strain along the kagome plane, *Phys. Rev. B* **106**, 195113 (2022).
- [53] V. M. Goldschmidt, Die gesetze der krystallochemie, *Naturwissenschaften* **14**, 477 (1926).
- [54] S. Tateno, K. Hirose, N. Sata, and Y. Ohishi, High-pressure behavior of  $\text{MnGeO}_3$  and  $\text{CdGeO}_3$  perovskites and the post-perovskite phase transition, *Phys. Chem. Miner.* **32**, 721 (2006).
- [55] K. Hirose, Stability and equation of state of  $\text{MgGeO}_3$  post-perovskite phase, *Am. Mineral.* **90**, 262 (2005).
- [56] Y. Shirako, H. Kojitani, M. Akaogi, K. Yamaura, and E. Takayama-Muromachi, High-pressure phase transitions of  $\text{CaRhO}_3$  perovskite, *Phys. Chem. Miner.* **36**, 455 (2009).
- [57] M. O'Keeffe, B. G. Hyde, and J.-O. Bovin, Contribution to the crystal chemistry of orthorhombic perovskites:  $\text{MgSiO}_3$  and  $\text{NaMgF}_3$ , *Phys. Chem. Miner.* **4**, 299 (1979).



- [58] C. McDaniel and S. Schneider, Phase relations in the CaO-IrO<sub>2</sub>-Ir system in air, *J. Solid State Chem.* **4**, 275 (1972).
- [59] T. Tsuchiya and J. Tsuchiya, Structure and elasticity of *Cmcm* CaIrO<sub>3</sub> and their pressure dependences: *Ab initio* calculations, *Phys. Rev. B* **76**, 144119 (2007).
- [60] D. Grohol, K. Matan, J. H. Cho, S. H. Lee, J. W. Lynn, D. G. Nocera, and Y. S. Lee, Spin chirality on a two-dimensional frustrated lattice, *Nat. Mater.* **4**, 323 (2005).
- [61] K. Matan, T. Ono, G. G. G. Gitgeatpong, K. de Roos, P. Miao, S. Torii, T. Kamiyama, A. Miyata, A. Matsuo, K. Kindo, S. Takeyama, Y. Nambu, P. Piyawongwatthana, T. J. Sato, and H. Tanaka, Magnetic structure and high-field magnetization of the distorted kagome lattice antiferromagnet Cs<sub>2</sub>Cu<sub>3</sub>SnF<sub>12</sub>, *Phys. Rev. B* **99**, 224404 (2019).
- [62] H. Kawamura and S. Miyashita, Phase transition of the two-dimensional Heisenberg antiferromagnet on the triangular lattice, *J. Phys. Soc. Jpn.* **53**, 4138 (1984).
- [63] M. I. Hussein, M. J. Leamy, and M. Ruzzene, Dynamics of phononic materials and structures: Historical origins, recent progress, and future outlook, *Appl. Mech. Rev.* **66**, 040802 (2014).
- [64] F. Warmuth, M. Wormser, and C. Körner, Single phase 3D phononic band gap material, *Sci. Rep.* **7**, 3843 (2017).
- [65] X. Gu and R. Yang, Phonon transport in single-layer transition metal dichalcogenides: A first-principles study, *Appl. Phys. Lett.* **105**, 131903 (2014).
- [66] U. Argaman, R. E. Abutbul, Y. Golan, and G. Makov, Phonon band gaps in the IV-VI monochalcogenides, *Phys. Rev. B* **100**, 054104 (2019).
- [67] G. Xu, B. Lian, and S.-C. Zhang, Intrinsic Quantum Anomalous Hall Effect in the Kagome Lattice Cs<sub>2</sub>LiMn<sub>3</sub>F<sub>12</sub>, *Phys. Rev. Lett.* **115**, 186802 (2015).
- [68] C.-L. Zhang, C. M. Wang, Z. Yuan, X. Xu, G. Wang, C.-C. Lee, L. Pi, C. Xi, H. Lin, N. Harrison, H.-Z. Lu, J. Zhang, and S. Jia, Non-saturating quantum magnetization in Weyl semimetal TaAs, *Nat. Commun.* **10**, 1028 (2019).
- [69] L. Ye, M. Kang, J. Liu, F. von Cube, C. R. Wicker, T. Suzuki, C. Jozwiak, A. Bostwick, E. Rotenberg, D. C. Bell, L. Fu, R. Comin, and J. G. Checkelsky, Massive Dirac fermions in a ferromagnetic kagome metal, *Nature (London)* **555**, 638 (2018).
- [70] K. Kuroda, T. Tomita, M. T. Suzuki, C. Bareille, A. A. Nugroho, P. Goswami, M. Ochi, M. Ikhlas, M. Nakayama, S. Akebi, R. Noguchi, R. Ishii, N. Inami, K. Ono, H. Kumigashira, A. Varykhalov, T. Muro, T. Koretsune, R. Arita, S. Shin *et al.*, Evidence for magnetic Weyl fermions in a correlated metal, *Nat. Mater.* **16**, 1090 (2017).
- [71] The anomalous Hall conductivity component,  $\sigma_{xy}$  for example, has been computed by the formula:
- $$\sigma_{xy} = -\frac{e^2}{\hbar} \int_{BZ} \frac{d^3\mathbf{k}}{(2\pi)^3} \Omega_{xy}(\mathbf{k}),$$
- where  $\Omega_{xy}(\mathbf{k}) = \sum_n^{occ} f_n(\mathbf{k}) \Omega_{n,xy}(\mathbf{k})$  is the summation of all the occupied  $n$  number of bands and  $f_n(\mathbf{k})$  is the Fermi distribution. Moreover, the symmetry-allowed AHC components, within the  $\Gamma_{4g}$  magnetic ordering, are:
- $$\sigma_{\Gamma_{4g}} = \begin{pmatrix} 0 & \sigma_{xy} & -\sigma_{xy} \\ -\sigma_{xy} & 0 & \sigma_{xy} \\ \sigma_{xy} & -\sigma_{xy} & 0 \end{pmatrix}$$
- [72] The AHC tensors in the  $\Gamma_{6g,y}$  and  $\Gamma_{6g,x}$  symmetries are:
- $$\sigma_{\Gamma_{6g,y}} = \begin{pmatrix} 0 & \sigma_{xy} & -\sigma_{xy} \\ -\sigma_{xy} & 0 & \sigma_{xy} \\ \sigma_{xy} & -\sigma_{xy} & 0 \end{pmatrix}$$
- $$\sigma_{\Gamma_{6g,x}} = \begin{pmatrix} 0 & 0 & -\sigma_{zx} \\ 0 & 0 & -\sigma_{zx} \\ \sigma_{zx} & \sigma_{zx} & 0 \end{pmatrix}$$
- [73] J. Kübler and C. Felser, Non-collinear antiferromagnets and the anomalous Hall effect, *Europhys. Lett.* **108**, 67001 (2014).
- [74] D. Boldrin, I. Samathrakris, J. Zemen, A. Mihai, B. Zou, F. Johnson, B. D. Esser, D. W. McComb, P. K. Petrov, H. Zhang, and L. F. Cohen, Anomalous Hall effect in noncollinear antiferromagnetic Mn<sub>3</sub>NiN thin films, *Phys. Rev. Mater.* **3**, 094409 (2019).
- [75] G. Gurung, D.-F. Shao, T. R. Paudel, and E. Y. Tsymbal, Anomalous Hall conductivity of noncollinear magnetic antiperovskites, *Phys. Rev. Mater.* **3**, 044409 (2019).
- [76] A. Pulkkinen, B. Barbiellini, J. Nokelainen, V. Sokolovskiy, D. Baigutlin, O. Miroshkina, M. Zagrebin, V. Buchelnikov, C. Lane, R. S. Markiewicz, A. Bansil, J. Sun, K. Pussi, and E. Lähderanta, Coulomb correlation in noncollinear antiferromagnetic  $\alpha$ -Mn, *Phys. Rev. B* **101**, 075115 (2020).
- [77] D. R. Baigutlin, V. V. Sokolovskiy, O. N. Miroshkina, M. A. Zagrebin, J. Nokelainen, A. Pulkkinen, B. Barbiellini, K. Pussi, E. Lähderanta, V. D. Buchelnikov, and A. T. Zayak, Electronic structure beyond the generalized gradient approximation for Ni<sub>2</sub>MnGa, *Phys. Rev. B* **102**, 045127 (2020).
- [78] G. Sai Gautam and E. A. Carter, Evaluating transition metal oxides within DFT-SCAN and SCAN +  $U$  frameworks for solar thermochemical applications, *Phys. Rev. Mater.* **2**, 095401 (2018).